Revealing the Elusive Structure and Reactivity of Iron Boride α-FeB

Fernando Igoa Saldaña, Emile Defoy, Daniel Janisch, Gwenaëlle Rousse, Pierre-Olivier Autran, Anissa Ghoridi, Amandine Séné, Marzena Baron, Leopoldo Suescun, Yann Le Godec, et al.

Revealing the elusive structure and the reactivity of iron boride α-FeB

Fernando Igoa,[1,2] Emile Defoy,[1] Daniel Janisch,[1] Gwenaëlle Rousse,[3] Pierre-Olivier Autran,[4] Anissa Ghoridi,[1] Amandine Séné,[1] Marzena Baron,[1] Leopoldo Suescun,[5] Yann Le Godec,[2] David Portehault[1*]

1 Sorbonne Université, CNRS, Laboratoire de Chimie de la Matière Condensée de Paris (CMCP), 4 place Jussieu, F-75005, Paris, France

2 Sorbonne Université, CNRS, MNHN, IRD, Institut de Minéralogie, de Physique des Matériaux et de Cosmochimie (IMPMC), 4 place Jussieu, F-75005, Paris, France

3 Collège de France, Sorbonne Université, Chimie du Solide et de l'Energie (CSE), 75231 Paris Cedex 05, France

4 European Synchrotron Radiation Facility, 71 Avenue des Martyrs, 38040 Grenoble, France

5 Cryssmat-Lab, DETEMA, Facultad de Química, Universidad de la República, Montevideo, Uruguay.

*Corresponding author: david.portehault@sorbonne-universite.fr

Abstract

Crystal structures can strongly deviate from bulk states when confined into nano-domains. These deviations may deeply affect properties and reactivity, and then call for a close examination. In this work, we address the case where extended crystal defects spread through a whole solid and then yield an aperiodic structure and specific reactivity. We focus on iron boride α-FeB, whose structure has not been elucidated yet, thus hindering the understanding of its properties. We synthesize the two known phases α-FeB and β-FeB in molten salts at 600 and 1100 °C, respectively. The experimental X-ray diffraction (XRD) data cannot be satisfyingly accounted for by a periodic crystal structure. We then model the compound as a stochastic assembly of layers of two structure-types. Refinement of the powder XRD pattern by considering the explicit scattering interference of the different layers allows quantitative evaluation of the size of these domains and of the stacking faults between them. We therefore demonstrate that α-FeB is an intergrowth of nanometer-thick slabs of two structure types: β-FeB and CrB-type structures, in similar proportions. We finally discuss the implications of this novel structure on the reactivity of the material and its ability to perform insertion reactions, by comparing the reactivities of α-FeB and β-FeB as reagents in the synthesis of a model layered material: Fe_2AlB_2. By using synchrotron-based *in situ* X-ray diffraction, we elucidate the mechanisms of formation of Fe_2AlB_2. We highlight the higher reactivity of the intergrowth α-FeB, in agreement with structural relationships.

Introduction

Nanoscale solids can yield large deviations of crystal structures compared to bulk states: as a result of the interface energy contribution to the overall energy landscape, nano-domains can accommodate larger strains,[1] deviate from bulk compositions,[2] and even show size-dependent polymorphism.[3] The latter has been known for decades in the case of oxides, where ϵ-Fe_2O_3,[4] λ-Ti_3O_5,[5] bixbyite-V_2O_3,[6] and more recently ϵ'-$Li_xV_2O_5$[7] could be isolated as a consequence of their low surface energy. These materials show unique properties for magnetic storage and shielding,[4] light-driven information storage,[5] oxygen storage,[6] and Li-ion batteries,[7] respectively. Fewer examples pertain to non-oxides, with the notable cases of cubic $Pb_{2-x}Sn_xS_2$[8] and of $Pb_mSb_{2n}Te_{m+3n}$ nanocrystals that enhance thermoelectric energy conversion.[9] CdSe nanoparticles also exhibit structure, morphology and defect-dependent optical properties.[10] Especially, a high density of stacking faults explains the unusual white light emission of ultra-small CdSe nanoparticles.[11] The confinement of solids into nano-domains can then yield specific structures that require close examination to interpret unique properties.

Iron borides have been extensively investigated for structural[12,13] and functional[14–16] applications. Beyond Fe-B alloying, multiple stoichiometric compounds are known, with compositions ranging from Fe_9B to FeB_{49}.[17] When manufactured at the nanoscale, iron borides exhibit distinct properties: FeB_2 nanoparticles are bifunctional electrocatalysts for overall water splitting surpassing the Pt/RuO_2 benchmark,[18] FeB nanoparticles are harder magnets than their bulk analogues.[19,20] Besides, the high temperature form of FeB, β-FeB, is also an efficient precursor for the synthesis of the MAB phase Fe_2AlB_2,[21–27] which is a potential magnetic cooler material[21] and a precursor to two-dimensional MBenes.[28–35 36] While the reactivity of β-FeB is well documented and rationalized at the atom-scale,[37,38] its low temperature counterpart, α-FeB,[16,19,20,39–41] remains elusive: its reactivity and properties have been seldom documented,[19,20] which is linked to the lack understanding of its atom-scale structure.[19]

There are strong hints that α-FeB is a modification at the nanoscale of the β-FeB structure displayed in **Figure 1a-b**. First, the X-ray diffractogram of α-FeB resembles that of β-FeB, with the exception of some missing diffraction lines and the presence of a broad diffuse scattering signal.[19] Second, transmission electron microscopy images of α-FeB particles exhibit contrasted parallel stripes.[20] The same streaks are observed only in nano-domains (30 — 100 nm) of β-FeB.[19,20,39–41] Three hypotheses have been proposed to account for the elusive structure of α-FeB:[19,20,39–45] **(i)** antisite mixing between Fe and B atoms;[46] **(ii)** crystallization in a higher symmetry space group (S.G.);[47] **(iii)** intergrowth through stacking faults between two structure-types.[48] Notwithstanding, none of these attempts has provided a satisfactory solution able to reproduce experimental diffractograms.

In the present work, we study an α-FeB material synthesized in molten salts. We analyze the different hypotheses of structural order by means of conventional powder diffraction modelling and refinement. The planar defects proposed in hypothesis **(iii)** above cannot be averaged in a long-range periodic structure, and thus cannot be accounted for by classical diffraction analysis techniques. We then study powder X-ray diffraction patterns through the elaboration and refinement of a statistical layered model to account for the occurrence of stacking faults.[49,50] We show that this approach can accurately and quantitatively describe disorder and bidimensional defects. We then reveal the atom-scale and nano-scale structure of α-FeB and demonstrate its potential as a precursor for the synthesis of model layered materials like Fe_2AlB_2.

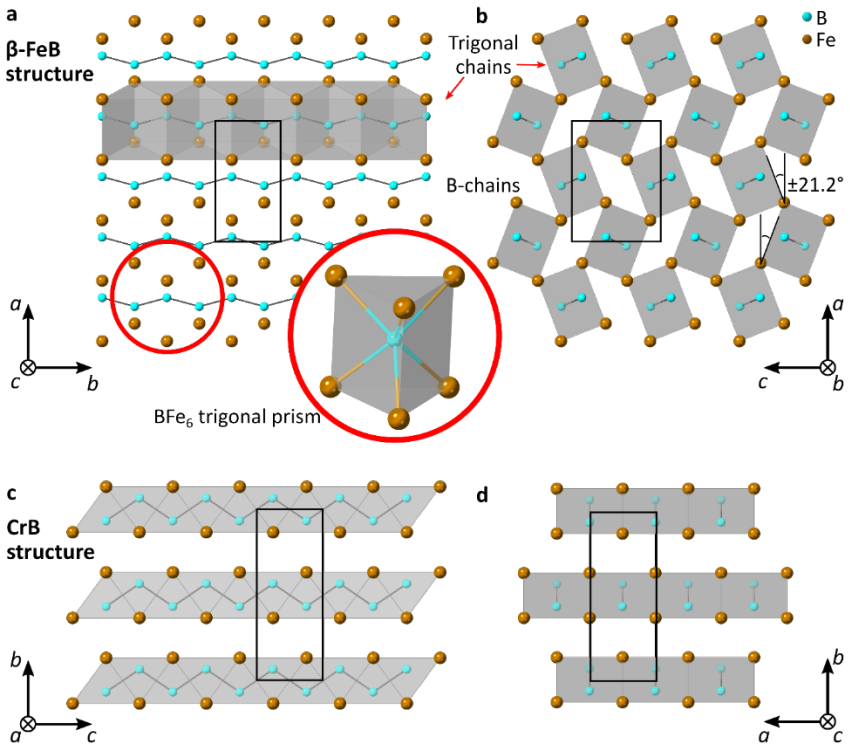

Figure 1. (a) Structure of β-FeB projected along the *ab* plane, main structural features are highlighted: BFe_6 trigonal prisms, B-chains and trigonal chains. The latter are the linear rectangular face-sharing arrangement of the BFe_6 trigonal prisms. (b) Structure of β-FeB projected along the ac plane showing the edge-sharing piling of the trigonal chain. (c) Structure of FeB in the CrB-type structure, suggested by Barinov *et al.*,[47] projected along the (c) *bc* and (d) *ab* planes. BFe_6 trigonal prisms in the CrB structure-type share both the rectangular and triangular faces to form bidimensional Fe_2B_2 sheets.

Experimental section

Materials

All reagents were stored and handled under an argon-filled glove box. $NaBH_4$ (98 % min., Alfa Aesar), $NaAlCl_4$ (99.9%, Alfa Aesar), and $FeCl_2$ (99.5%, Alfa Aesar) were used as B, Al and Fe sources, respectively. NaH (90 %, Aldrich) was used as reducing agent. All reagents were used as received. A eutectic mixture of LiCl (99.9% Alfa Aesar)/KCl (99.9% Sigma Aldrich) (45:55 *wt*. %) was used as solvent. Deionized H_2O or MeOH (VWR Normapur grade) were used for washing steps.

Methods

The heat treatments were performed in vertical tubular ovens connected to temperature controllers from Eraly®. These ovens were calibrated every 100 °C between 100 and 1100 °C. The temperatures we indicate are the effective temperatures in the synthesis crucible.

Synthesis of α-FeB and β-FeB

850 mg (6.71 mmol) of $FeCl_2$ and 254 mg (6.71 mmol) of $NaBH_4$ were mixed with 5.1 g of the eutectic LiCl/KCl mixture. All solids were finely ground together at 20 Hz for 2 min in a Retsch MM400 ballmiller (airtight vials of 50 mL, one steel ball of 62.3 g and a diameter of 23 mm). The solid mixture was later placed in a Mo crucible (Ø15 × H200 mm), which was placed into a sealed quartz tube. The quartz tube was connected to a Schlenk line under Ar flow and placed inside a vertical oven. A heating ramp of $10°C \cdot min^{-1}$ was used up to 600 °C for α-FeB and 1100 °C for β-FeB, followed by a dwell time of 3 h. We also tested different dwell times from 0.5 h to 12 h, and did not observe a significant effect of this parameter. After dwelling, the sample was let to cool down naturally and subsequently washed with methanol by sequences of redispersion, sonication (1 min) and magnetic separation of the solid, until the conductivity of the supernatant dropped below 50 $\mu S \cdot cm^{-1}$. Methanol-washed samples required preliminary grinding of the solidified mixture in order to extract the product due to the low solubility of the salt in the solvent. The powders were dried under vacuum at room temperature until the pressure dropped below $1.0 \cdot 10^{-3}$ mbar and were then heated to 150 °C with an oil bath still under vacuum overnight.

Synthesis of Fe_2AlB_2

Impregnation of FeB. In order to optimize the reactivity of FeB particles, they were pre-dispersed in the eutectic salt mixture before melting. To do so, 62 mg (0.925 mmol) of FeB (either the α or β modifications) were placed in a Schlenk tube and connected to a Schlenk line. 1 mL of methanol was added and the suspension sonicated for 20 min to assure proper dispersion. Then, 2.55 g of previously ground LiCl/KCl were added abruptly. The mixture was then evacuated under vacuum, first at room

temperature and then in a stepwise heating to 50, 75, 100, 120 and finally 150 °C. Each heating step was maintained until the vacuum pressure dropped below 10^{-2} mbar, except the final step (150 °C) that was maintained until the vacuum pressure dropped below $1.0 \cdot 10^{-3}$ mbar.

Final mixing and synthesis. Impregnated FeB and LiCl/KCl were mixed with of 266 mg $NaAlCl_4$ (1.388 mmol), 111 mg of NaH (4.625 mmol) and 2.55 g more of LiCl/KCl eutectic mixture. All solids were finely ground together at 20 Hz for 2 min in a Retsch MM400 ballmiller (airtight vials of 50 mL, one steel ball of 62.3 g and a diameter of 23 mm). The solid mixture was later placed in a Mo crucible (Ø15 × H200 mm), which was placed into a quartz tube. The quartz tube was connected to a Schlenk line under Ar flow and placed inside a vertical oven. A heating ramp of $10°C \cdot min^{-1}$ was used up to 1000 °C, followed by a dwell time of 1 h. After dwelling, the sample was let to cool down naturally and subsequently washed in sequences of solvent mixing, sonication (1 min), centrifugation at 21000 RPM for 2 min and separation of the solid, until the conductivity of the supernatant dropped below 50 $\mu S \cdot cm^{-1}$. The powder was dried under vacuum at 60 °C overnight.

Characterization

Powder X-ray diffraction patterns were collected in a Bruker D8 Discover diffractometer, with a theta-theta Bragg-Brentano geometry and Ni-filtered CuK_α sealed-tube radiation source ($\lambda_{average}$ = 1.5418 Å) operating at 40kV/30mA. The diffractometer radius is 280 mm.The X-ray intensity was measured by 9.2 s collection steps of $\Delta 2\theta$ = 0.0128°. Diffracted intensity was collected using a LynxEye linear detector. The reference crystallographic structure of β-FeB and CrB structures were taken from the ICSD database (391329 and 44249 cards respectively), while $Al(OH)_3$, $Al_{9.75}Fe_3$, Fe_3Al and Fe_2AlB_2 references were taken from the PDF-4+ database (00-020-0011, 01-082-9854, 00-050-0955 and 04-007-5354 cards, respectively). Rietveld refinements were performed using the GSAS-II software.[51] Stacking faults modelling and refining was performed using the FAULTS software.[49,50]

Transmission electron microscopy analyzes were performed in a Tecnai Spirit 2 apparatus, equipped with a LaB_6 electron gun, operating at 120 kV. Samples were dispersed by sonication on ethanol and deposited on top of Cu grids covered with a carbon membrane.

***In situ* angular X-ray diffraction** was carried out at the ESRF synchrotron, on the ID11 beamline, in transmission mode at a fixed energy (wavelength) of 93.3159 keV (0.1329 Å). A Double Crystal Monochromator equipped with two Si(111) crystals was used to tune the energy and the beam size was set to 300x300 microns. The detector was a Frelon4M 2048x2048 16Bit fast CCD Camera. We used

a homemade capillary oven. In brief, it enables performing transmission X-ray diffraction *in situ* during controlled heating of the reaction mixture in a 1.5 mm-diameter quartz capillary opened under argon flow, to mimic the conditions of *ex situ* lab synthesis.

Results and discussion

Synthesis of α-FeB and β-FeB

FeB was synthesized by adapting a previously reported synthesis in molten salts:[52,53] iron chloride acts as metal precursor and $NaBH_4$ as both reducing agent and boron source, according to **Equation 1**. The eutectic LiCl/KCl mixture was chosen as a cheap, polar and low-melting point solvent (347°C) to trigger reactions in the liquid state. The powders were mixed at room temperature and heated under argon flow. After cooling, the powders were washed with methanol. X-ray diffraction patterns (**Figure 2**) indicate that α- and β-FeB are obtained for syntheses at 600 and 1100°C, respectively. Especially, we recognize the XRD pattern of α-FeB from the typical absences of the $(101)_\beta$, $(201)_\beta$, $(111)_\beta$, $(211)_\beta$ and $(301)_\beta$ reflections (shown in red indexes in **Figure 2**, the β subindex in the crystallographic planes and directions' notation refers to the β-FeB structure, in contrast to the CrB subindex used later, referring to the CrB-structure type) of the β-FeB pattern, as well as the broad diffuse scattering at 2θ (CuK_α) ≈ 41°.[19] No crystalline oxidized species could be detected by XRD (**Figure 1a**) in the corresponding products, which contain mostly α/β-FeB as crystalline phases. No amorphous oxides were observed by TEM (**Figure 3a**-**b**), but the β-FeB sample contains traces of Fe_2B impurities. The characteristic parallel stripes of α-FeB are recognized in TEM images (**Figure 3**).

$$FeCl_2(s) + NaBH_4(s) \rightarrow FeB(s) + 1.5\ H_2(g) + NaCl(s) + HCl(g) \quad (1)$$

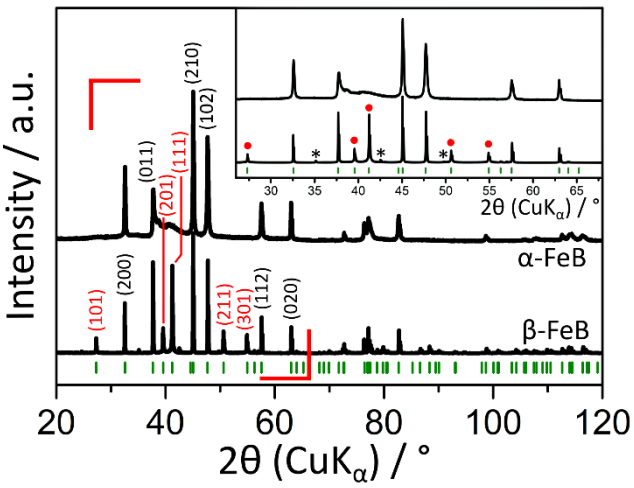

Figure 2. Powder XRD diffractograms of α- and β-FeB products synthesized in molten salts at 600 and 1100 °C, respectively, and washed with methanol. The expected Bragg positions for the β-FeB structure are marked with green stripes. Miller indexes marked in red correspond to the characteristic absences of β-FeB reflections in α-FeB. *Inset:* Magnification of the diffraction patterns in the framed region, characteristic absences in α-FeB are marked with red dots, Fe_2B traces are marked with *.

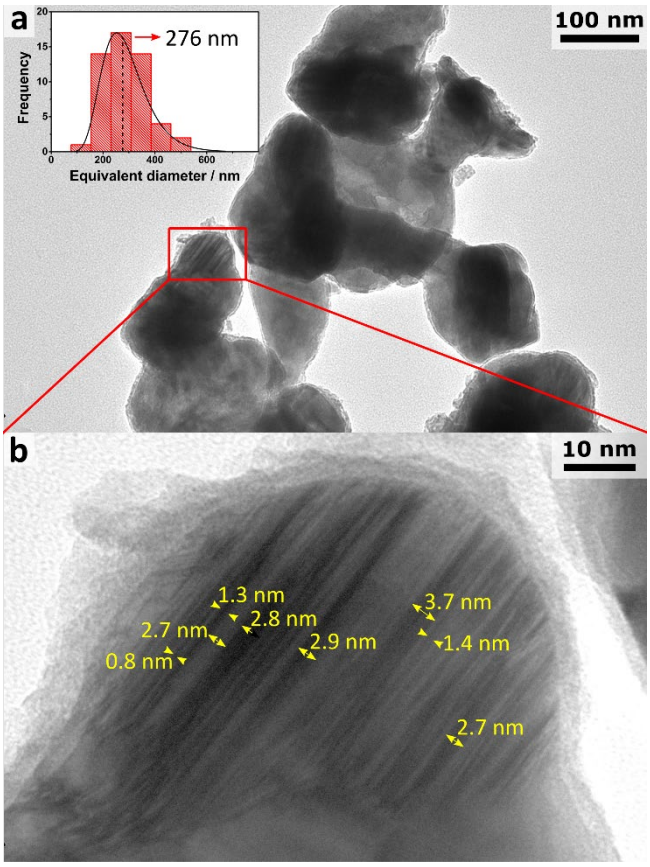

Figure 3. TEM micrographs of α-FeB. Inset in (a) shows the corresponding size distribution histogram. (b) A higher magnification of a particle highlights streaks with varying contrasts and an average thickness of ~ 2 nm. These features are characteristic of the α-FeB structure.[20]

β-FeB crystallizes in the orthorhombic *Pnma* space group (*a* = 5.4954 Å, *b* = 2.9408 Å, *c* = 4.0477 Å), where both Fe and B occupy the *4c* Wyckoff position (**Figure 1**).[54] Its most prominent structural features are the BFe_6 trigonal prismatic units (**Figure 1a** inset), which share faces. These units form boron chains in trans configuration, as commonly observed for many other B-rich compounds.[55,56] The ensemble of the B-chains and its coordinated Fe atoms (named trigonal chains hereafter) extend along the $[010]_\beta$ direction (**Figure 1a**). The trigonal chains are packed along the $[100]_\beta$ direction by sharing edges (**Figure 1b**). All units are tilted along the $[010]_\beta$ direction by alternating angles of ± 21.2° *versus* the *a* axis (**Figure 1b**). On the other side, the structure of α-FeB is believed to be related to β-FeB due to the similarities of the powder patterns. To decipher its actual crystal structure, we analyze below the hypothesis raised in previous works.

Structure analysis of α-FeB

Hypothesis (i): Fe/B antisite mixing

Fruchart proposed partial anti site mixing of Fe and B, resulting in mixed occupations of the Fe and B positions.[46] This hypothesis is likely unreliable as the Fe-Fe distance would drop below that of elemental iron (2.15 Å against 2.84 Å respectively) and boron covalent chains would be broken, [19,40,48] which would impact the Curie temperature, contrary to observations.[48] Besides, models of Fe/B antisite mixing $(Fe_xB_{1-x})\_4c$ $(B_xFe_{1-x})\_4c$ every 10 % exchange (**Figure S1a**) do not enable reproducing the experimental diffractogram. Rietveld refinement by also allowing asymmetric substitutions and the presence of vacancies (**Figure S1b** and **Table 1**) could not reach satisfactory agreement with the experimental pattern. All in all, we discard the hypothesis of Fe/B substitution.

Table 1. Summary of crystallographic parameters for the refinement of all the models studied for α-FeB. In the case of the phase mixture model, only the β-FeB structure parameters are shown.

Hypothesis:	**(i)**	**(ii)**		**(iii)**	
Model:	**Anti-site mixing**	**S.G. *Cmcm***	**S.G. *Pnca***	**Phase mixture**	**Intergrowth**
a (Å)	5.4954(2)	2.9460(4)	5.4944(4)	5.49312(3)	5.4989(2)
b (Å)	2.9492(3)	7.6100(3)	2.9491(2)	2.94817(4)	2.9505(3)
c (Å)	4.0622(2)	2.9491(2)	4.0614(3)	4.06097(5)	4.0641(2)
Volume ($Å^3$)	65.961(8)	66.130(10)	65.808(8)	65.766(13)	65.961(8)
R_{wp} (%)	52.8	49.9	33.3	35.1	7.4
χ^2	604.50	549.40	245.10	267.34	18.72

Hypothesis (ii): Crystallization in the CrB-type structure (S.G. *Cmcm*)

Barinov *et al.* proposed that the higher symmetry space group *Cmcm* under the lattice parameters *a* = 2.954 Å, *b* = 7.564 Å, *c* = 2.953 Å was responsible for imposing systematic absences in α-FeB compared

to the ideal β-FeB structure (S.G. *Pnma*).[47] The *Cmcm* and the *Pnma* space groups are linked by a group-subgroup relation, for which the axis in *Cmcm* relate to those of *Pnma* as: $a_{Cmcm} = b_{Pnma}$, $b_{Cmcm} = c_{Pnma}$ and $c_{Cmcm} = a_{Pnma}$. This allows to compare the lattice parameters, which remain almost unaltered for b_{Pnma} (2.9408 Å *vs*. 2.954 Å in a_{Cmcm}), while c_{Pnma} expands from 4.0477 Å to 7.564 Å in b_{Cmcm}, as in the latter it corresponds to the stacking direction of the trigonal layers. This expansion is compensated by the contraction of the a_{Pnma} by approximately the same amount, which in turn yields similar cell volumes: V_{Pnma} = 65.414 Å *vs*. V_{Cmcm} = 65.982 Å. The increase in symmetry would then yield the CrB-type structure, shown in **Figure 1c-d**.[47] This model is indeed closely related to the β-FeB structure and made of the same building units: BFe_6 trigonal prismatic units. In the CrB-type structure, the trigonal chains extend along the $[001]_{CrB}$ direction and exhibit a face-sharing planar packing in the $[100]_{CrB}$ direction, the layers are then piled along the $[010]_{CrB}$ direction.

For their analysis, Barinov *et al.* relied on a highly strained sample characterized by the large width of the diffraction peaks.[47] Our synthesis procedure yields samples with higher crystallinity. The thinner diffraction peaks offer better resolved experimental data to test hypothesis **(ii)**. Rietveld refinement using the cell previously proposed structure as starting model does not yield a satisfactory fit, neither did manual increasing nor decreasing of the lattice parameters. The best fit, yielding lattice parameters *a* = 2.9460(4) Å, *b* = 7.6100(3) Å, *c* = 2.9491(2) Å, is shown in **Figure S2a** and the retrieved crystallographic parameters summarized in **Table 1**.

By extending the proposition of Barinov *et al.*, we raised the question whether another space group could explain the reflection absences. For this reason, we have attempted to determine the unit cell and space group of α-FeB *ab initio* with the EXPO2014 software.[57] The most plausible model found was an orthorhombic cell of space group *Pbcn*. For direct comparison to the β-FeB structure, this space group is treated under the unconventional *Pnca* setting, with cell parameters: *a* = 5.498(4) Å, *b* = 2.951(18) Å, *c* = 4.062(2) Å. This model is very close to the reported β-FeB structure (S.G. *Pnma*, *a* = 5.495 Å, *b* = 2.941 Å, *c* = 4.057 Å), with the main difference being a *c* glide plane substituting the *m* mirror perpendicular to the *b* axis. The glide plane imposes the extra systematic absence of *h0l*: *l* = 2*n*, which in turn forbids the (101), (201) and (301) reflections. To further account for the remaining experimental absences, we attempted to solve the structure in this space group by direct methods, but could not reach any plausible result. Alternatively, we tested the assumption that the atoms would lie in the same positions than in β-FeB given the similarity of the cell metrics and the fact that α-FeB transitions to β-FeB under thermal treatment. In turn, placing Fe and B atoms in the original β-FeB positions does extinguish the remaining $(111)_\beta$ and $(211)_\beta$ peaks. However, that is also true for the

experimentally observed $(011)_\beta$ reflection, which discards this atomic positioning. Refinement in general positions does not yield a plausible model nor does it reproduce the diffraction pattern (best fit shown in **Figure S2b** with crystallographic parameters in **Table 1**). No other proposed S.G. by EXPO2014 could account for the observed and missing reflections of α-FeB. Consequently, we discarded hypothesis **(ii)**.

Hypothesis (iii): Faulted intergrowth of the β-FeB and the CrB-type structures.

Kanaizuka suggested a recursive intergrowth between the CrB-type and β-FeB structures to model α-FeB.[48] The author relied on the earlier discoveries by Parthé and collaborators [58–62] that (a) several rare earth-metalloid alloys (DySi, HoSi, ErSi and PrGe) crystallized in the CrB structure at low temperature, which transitioned to the β-FeB structure upon heating, and that (b) β-FeB and CrB-type structures were intermixed in periodically faulted stacks in YNi and GdNi-DyNi. On these bases, Kanaizuka built a 4-layers model, whose binary intermixing renders either pure CrB-type, pure β-FeB or a mixed β-FeB/CrB structure (**Figure 4**).[48] The layers A-D (**Figure 4a**) are made from the unit cell of the original β-FeB structure with origin shifts in the *ab* plane such that they fit one on top of the other while keeping bond distances reasonable. **Figure 4b** indicates the resulting structures from the binary mixtures of these layers stacked along the $[100]_\beta$ axis. Kanaizuka[48] then computed the interferences of the scattered waves from each layer by considering their probabilities of existence $P_A = 0.55$ and $P_B = P_C = P_D = 0.15$, which could account for the change of relative intensities of the $(101)_\beta$, $(201)_\beta$, $(111)_\beta$, $(211)_\beta$ and $(301)_\beta$ reflections and for the two distinct crystallographic Fe positions identified by ^{57}Fe-Mössbauer spectra in α-FeB. However, the calculated diffractogram was still far from reproducing the experimental profile.[48,63]

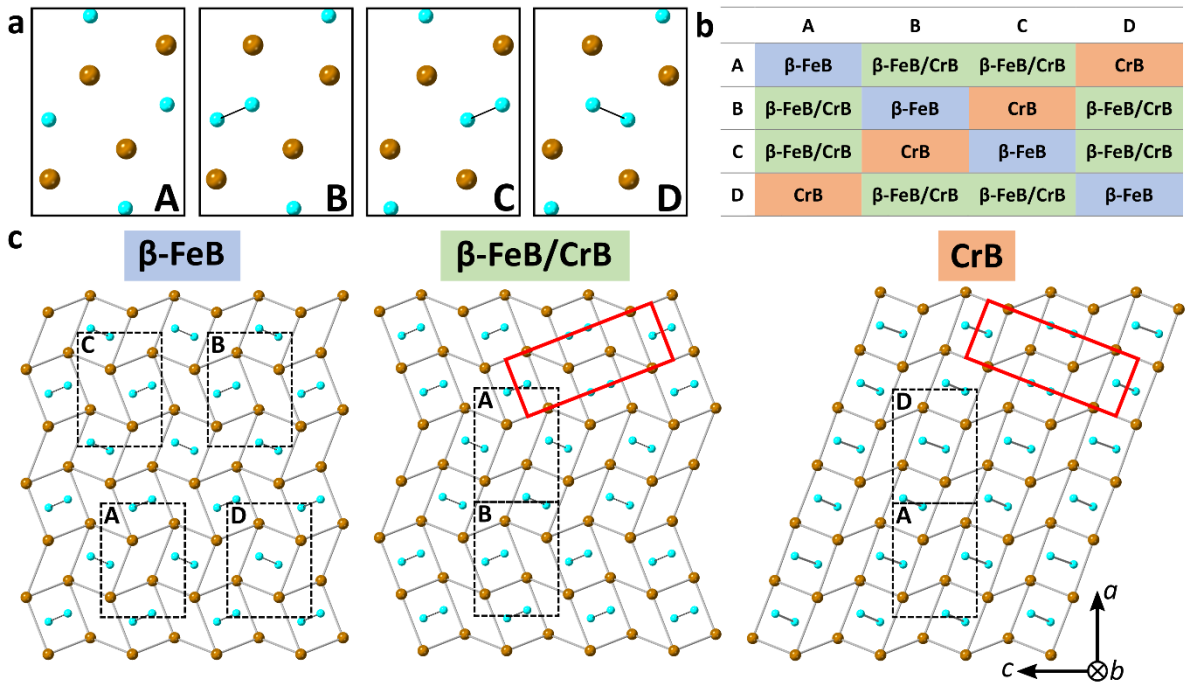

Figure 4. (a) The four possible layer-types according to Kanaizuka's model. (b) Possible binary combinations outcome. (c) Visualization of binary outcomes.[48]

Conventional Rietveld refinement cannot account for stochastic stacking faults, as it only considers periodic structures. However, following the original idea of Kanaizuka, the powder diffractogram can be simulated and refined based on the explicit interference from the scattering of each layer. The FAULTS software has been developed for this purpose[49,50] with high reliability for several types of materials.[64–67] FAULTS models the diffractogram by considering a probabilistic assembly of layers along defined stacking vectors. We define the structure from A, B, C and D layers as building blocks stacked along the $[100]_\beta$ vector, with probabilities α_{ji} to transition from a layer *j* to *i* (where *j* and *i* are A, B, C or D). The probabilities of transition relate to the probabilities of existence P_i through **Equations 2** and **3** below.[68] All symmetry elements but the identity are dropped as periodicity is no longer mandatory. The atomic coordinates are listed in **Table S1**. As in Rietveld refinement, FAULTS can also account for size broadening, occupations, Debye-Waller factors, atomic positions and unit cell variations, among others. This approach allows to describe bidimensional defects and disorder. Since the transition probabilities can be refined, we can then quantify the amount of each layer.

$$P_i = \sum_{j=1}^{N} P_j \alpha_{ji} \tag{2}$$

$$\sum_{i=1}^{N} P_i = 1 \tag{3}$$

For a first set of simulations and for the sake of simplicity, only two sets of binary combinations were considered, that is A/B and B/C, as they suffice to explore all binary outcomes (see **Figure 4b**). Transition probabilities were initially fixed to be equal for every arrival layer —$\alpha_{Ai} = \alpha_{Bi}$ or $\alpha_{Bi} = \alpha_{Ci}$ for i = A or B and B or C, respectively— and thus equal to the existence probability ($\alpha_{ji} = P_i$). Increments of 0.1 in existence probabilities were probed. The results can be seen in **Figure S3a** and **S3b** for the A/B and B/C binary combinations, respectively. One can readily observe that some combinations significantly reduce the intensities of the reflections missing in α-FeB. The case where $P_B = P_C = 0.5$ (marked in red in **Figure S3b**) stands out as all the $(101)_\beta$, $(201)_\beta$, $(111)_\beta$, $(211)_\beta$ and $(301)_\beta$ reflections vanish, in agreement with the experimental diagram. This strongly supports the hypothesis of CrB-type/β-FeB intergrowth by stacking faults along the $[100]_\beta$ axis, although the diffuse scattering is still not well modelled. Further simulations (**Figure S3d**) were carried out by fixing the existence probability $P_B = P_C = 0.5$ and by varying the transition probabilities α_{ji}, under the simplification hypothesis that transition probabilities are symmetric ($\alpha_{ji} = \alpha_{ij}$). The main effect observed is the modification of the diffuse scattering profile with α_{BB}, which at the limit of $\alpha_{BB} = \alpha_{CC} = 0$ and $\alpha_{BC} = \alpha_{CB} = 1$ transforms in the characteristic Bragg peaks of the CrB-type structure. Similar α_{ji} screening simulations were carried out for the A/B mixing system for comparison purposes (**Figure S3c**), where an analogous trend was observed. These first simulations were crucial to fix a plausible initial input model for the following refinements. The complete values of probabilities employed can be found in **Table S2**.

In order to reproduce the diffuse scattering and reach an overall satisfactory fit of the experimental pattern, we had to include all four layers and asymmetrical transition probabilities ($\alpha_{ji} \neq \alpha_{ij}$) throughout the FAULTS refinement. The final refinement is depicted in **Figure 5a** for a restricted 2θ range for clarity. And the crystallographic parameters summarized in **Table 1**. The recovered transition probabilities are summarized in the A_{ji} tensor in **Table S3**, and a representation of the complete 2θ range can be found in **Figure S4**. The powder diffractogram is very well reproduced, achieving figures of merits of R_{wp} = 7.3 % and χ^2 = 18.70. *Ergo*, our results confirm that α-FeB is an intergrowth of CrB-type and β-FeB structures stacked faults along the $[100]_\beta$ axis. This quantitative refinement permits to calculate the existence probabilities for the four types of layers: $P_A = 0.20$, $P_B = 0.33$, $P_C = 0.33$ and $P_D = 0.14$. Noteworthy, these values highly deviate from those initially proposed by Kanaizuka.[48] Rietveld refinement with a phase mixture of the CrB and β-FeB as model was also performed for comparison (**Figure 5b**). The difference in the modelling between Rietveld and FAULTS is evident and shows that α-FeB is an intimate intergrowth of the two structure types and not simply a phase mixture.

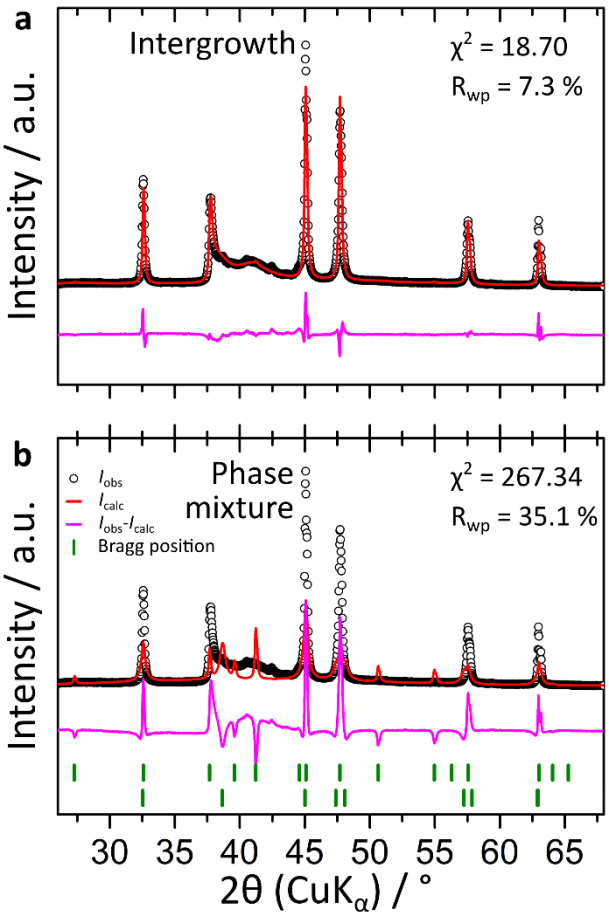

Figure 5. Different refinement approaches to model α-FeB. (a) FAULTS refinement with the 4-layers model proposed by Kanaizuka.[69] (b) Rietveld refinement of a phase mixture β-FeB/CrB-type structure.

The existence probabilities P_A, P_B, P_C and P_D and transition probabilities α_{ji} obtained from the FAULTS refinement can be converted into fractions of β-FeB and CrB domains. First, the existence probability of each binary combination of layer types (**Figure 4b**) is the existence probability of the departure layer (P_j) multiplied by the transition probability towards the arrival layer (α_{ji}). Then, one must consider the individual contributions of each binary combinations to each structure type. The combinations yielding pure β-FeB (see **Figure 4b**: A/A, B/B, C/C and D/D) and those yielding pure CrB (A/D, B/C, C/B, D/A) contribute only to β-FeB or CrB structure types, respectively. For each combination yielding mixed β-FeB/CrB (**Figure 4b**), 50 % of the combination corresponds to β-FeB and 50 % to CrB-type structure. Then the β-FeB cluster fraction is evaluated as the sum of the existence probabilities of pure β-FeB combinations plus half of the existence probabilities of β-FeB/CrB combinations. The CrB cluster fraction is calculated analogously. In the end, we evaluate β-FeB and CrB-type fractions at 0.57 and 0.43, respectively.

We further extended the analysis to assess the distribution of β-FeB and CrB domain sizes along the stacking direction. To do so, we adapted a model reported by Serrano-Sevillano and collaborators.[64] We generated a stochastic sequence of 100,000 layers following the transition probabilities α_{ji} obtained from the FAULTS refinement, in order to obtain statistically meaningful values of average domain size. For enhanced accuracy, the calculation is repeated for 20 sequences generated independently. We obtained average domain sizes of 2.5 and 2.1 nm for the β-FeB and CrB domains, respectively. These values are consistent with the thickness of the contrasted domains observed by TEM (**Figure 3**).

All in all, from the different models studied to explain the features of the α-FeB diffraction pattern (**Table 1**), the nanoscale intergrowth of α-FeB and CrB-type structures stands out for its consistency with experimental results.

α-FeB: new reagent towards Fe_2AlB_2

The lack of insights into its structure has hindered the study of the reactivity of α-FeB, while β-FeB is already known as precursor towards Fe_2AlB_2 (**Figures 1a-b** and **6b**),[37,38] our structure resolution shows that α-FeB is an intergrowth made of nano-domains of β-FeB and CrB-type structures. The CrB-type component of this intergrowth presents a clear structural relationship with Fe_2AlB_2 (**Figure 6**), which could ensure insertion of Al atoms to form Fe_2AlB_2, and thus easier conversion to this MAB phase. Overall, comparing the reactivity of α-FeB and β-FeB could highlight interesting effects of nanoscale domains and of crystal defects. We have then evaluated the possibility to use α-FeB in the synthesis of Fe_2AlB_2.

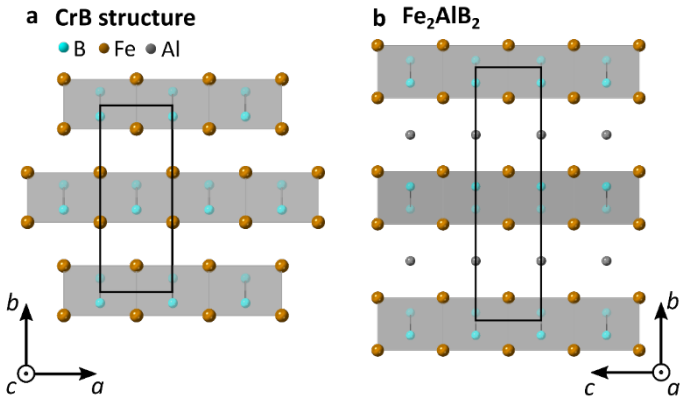

Figure 6. Structural relationship between the (a) CrB-type structure and (b) Fe_2AlB_2.

To target Fe_2AlB_2 from FeB phases, we have modified a recent synthesis in molten salts,[70] by using the LiCl/KCl eutectic mixture as solvent, $NaAlCl_4$ as an Al source, NaH as a reducing agent to generate *in situ* Al^0 (**Equations 4 and 5**), and α or β-FeB with molar ratios FeB:Al:NaH = 2:1.5:10. The large NaH

excess ensures fast delivery of Al atoms, while the excess of Al *versus* FeB fastens its incorporation, as previously reported.[37,38,70] In order to favor the Al incorporation, we have increased the surface of the FeB particles exposed to the reaction medium by developing an impregnation protocol. The particles were dispersed in methanol and then abruptly mixed with previously ground a LiCl/KCl eutectic salt mixture in order to avoid re-aggregation. If this step is by-passed, FeB is retrieved in the final product, up to a 20 % weight fraction.

$$NaAlCl_4(s) + 3\ NaH(s) \rightarrow Al(s) + 4\ NaCl(s) + 1.5\ H_2(g) \quad (4)$$

$$2\ FeB(s) + Al(s) \rightarrow Fe_2AlB_2(s) \quad (5)$$

Both α and β-FeB were reacted following the same protocol, by heating at 1000°C for 1 h. The XRD diagrams of the two resulting powders (**Figure S5**) exhibit reflections of Fe_2AlB_2 as major phase. However, α-FeB yielded a significantly higher purity of 61 wt. % *versus* only 43 wt. % when β-FeB was employed. This higher purity of the MAB phase can be linked to the insertion reaction that was expected from the structural similarity between the CrB-type component and the Fe_2AlB_2 product. To confirm this point, we assessed whether α-FeB transitioned through the high temperature β phase before formation of Fe_2AlB_2. We employed synchrotron-based *in situ* X-ray diffraction to probe this reaction mechanism, by acquiring an XRD pattern every minute in transmission mode through the reaction medium with a composition identical to the lab-scale synthesis. The diagrams are plotted against the reaction time as a heatmap in **Figure 7**. Al^0 forms at the expense of NaH at *ca*. 380°C, where the hydride is consumed to reduce Al^{3+} species. α-FeB remains up to ~ 845°C, when the Fe_2AlB_2 peaks appear. The peak position mismatch to the reference is attributed to thermal dilatation. No signs of the characteristic $(101)_\beta$, $(201)_\beta$, $(111)_\beta$, $(211)_\beta$ or $(301)_\beta$ reflections of β-FeB are detected, thus indicating a direct reaction from α-FeB to Fe_2AlB_2. The same experiment starting from β-FeB (**Figure S4**) shows an identical reaction sequence, at similar temperatures. This suggests that incorporation of Al atoms into the β-FeB nano-domains in α-FeB is a rate-limiting step for the overall reaction, which is consistent with a larger structural rearrangement required to transform into the Fe_2AlB_2 structure. The difference of grain sizes could also be at the origin of the reactivity difference, although this is unlikely as all FeB is consumed in both cases, suggesting that Al diffusion does note limit the reaction. Consequently, α-FeB could replace advantageously β-FeB as a precursor to produce Fe_2AlB_2, since it ensures higher Fe_2AlB_2 purity and can be produced at 400 °C against 1100 °C for β-FeB, thus ensuring lower energy consumption.

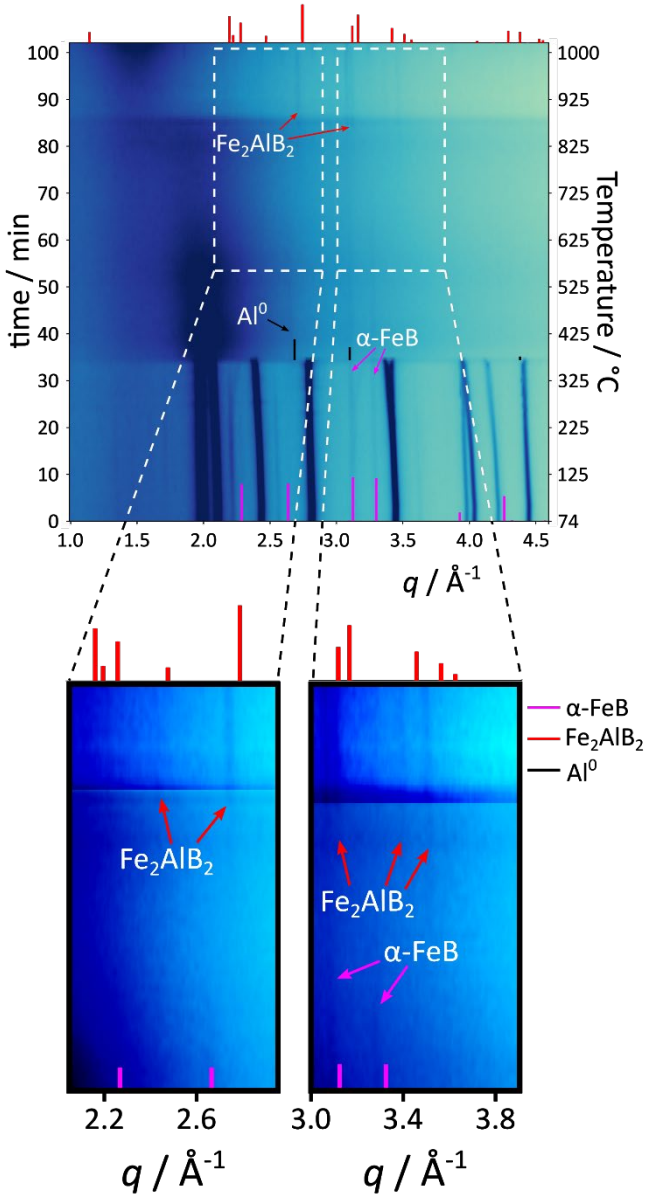

Figure 7. Synchrotron *in situ* XRD monitoring of the Fe_2AlB_2 synthesis from α-FeB in a molten salt.

Conclusions

Two structural modifications of FeB, α-FeB and β-FeB, have been selectively synthesized in molten salts at low and high temperature, respectively. We have demonstrated for the first time that α-FeB is an intergrowth of nano-domains of β-FeB and CrB structure types. The β-FeB and CrB domains are *ca*. 2 nm-thick slabs stacked along a common crystallographic axis and separated by stacking faults. This structure, combined with the nanoscale of the crystal domains and the possibility for these domains to undergo direct insertion reaction of Al, explains why α-FeB produced at low temperature is a more efficient precursor towards Fe_2AlB_2, although previous works had focused only on β-FeB. By addressing layered aperiodic structures in nano-objects, this work sheds light on the structure of faulted

nanoparticles of boron-based compounds and paves the way to the exploration of the chemical reactivity and physical properties of these solids.

Acknowledgements

The authors acknowledge the French Ministry for Research and the Doctoral School ED397 for funding of F.I. This work has been supported by the European Research Council (ERC) Consolidator Grant GENESIS under the European Union's Horizon 2020 research and innovation program (grant agreement n° 864850). *In situ* XRD was performed at ESRF under the proposal MA-5188 and received financial support from the ESRF.

References

(1) Gilbert, B.; Huang, F.; Zhang, H.; Waychunas, G. A.; Banfield, J. F. Nanoparticles: Strained and Stiff. *Science* **2004**, *305*, 651–654.

(2) Delacroix, S.; Igoa, F.; Song, Y.; Le Godec, Y.; Coelho-Diogo, C.; Gervais, C.; Rousse, G.; Portehault, D. Electron Precise Sodium Carbaboride Nanocrystals from Molten Salts: Single Sources to Boron Carbides. **2021**, *60*, 4252. https://doi.org/10.1021/acs.inorgchem.0c03501.

(3) Christiansen, T. L.; Bøjesen, E. D.; Juelsholt, M.; Etheridge, J.; Jensen, K. M. Ø. Size Induced Structural Changes in Molybdenum Oxide Nanoparticles. *ACS Nano* **2019**, *13*, 8725–8735. https://doi.org/10.1021/acsnano.9b01367.

(4) Tuček, J.; Zbořil, R.; Namai, A.; Ohkoshi, S. I. ε-Fe2O3: An Advanced Nanomaterial Exhibiting Giant Coercive Field, Millimeter-Wave Ferromagnetic Resonance, and Magnetoelectric Coupling. *Chemistry of Materials* **2010**, *22* (24), 6483–6505. https://doi.org/10.1021/cm101967h.

(5) Ohkoshi, S. I.; Tsunobuchi, Y.; Matsuda, T.; Hashimoto, K.; Namai, A.; Hakoe, F.; Tokoro, H. Synthesis of a Metal Oxide with a Room-Temperature Photoreversible Phase Transition. *Nature Chemistry* **2010**, *2* (7), 539–545. https://doi.org/10.1038/nchem.670.

(6) Bergerud, A.; Buonsanti, R.; Jordan-Sweet, J. L.; Milliron, D. J. Synthesis and Phase Stability of Metastable Bixbyite V2O3 Colloidal Nanocrystals. *Chemistry of Materials* **2013**, *25* (15), 3172–3179. https://doi.org/10.1021/cm401530t.

(7) Luo, Y.; Bai, Y.; Mistry, A.; Zhang, Y.; Zhao, D.; Sarkar, S.; Handy, J. V; Rezaei, S.; Chihpin Chuang, A.; Carrillo, L.; Wiaderek, K.; Pharr, M.; Xie, K.; Mukherjee, P. P.; Xu, B.-X.; Banerjee, S. Effect of Crystallite Geometries on Electrochemical Performance of Porous Intercalation Electrodes by Multiscale Operando Investigation. *Nature Materials* **2022**, *21*, 217–227. https://doi.org/10.1038/s41563-021-01151-8.

(8) Soriano, R. B.; Malliakas, C. D.; Wu, J.; Kanatzidis, M. G. No Title. *Journal of the American Chemical Society* **2012**, *134*, 3228.

(9) Soriano, R. B.; Arachchige, I. U.; Malliakas, C. D.; Wu, J.; Kanatzidis, M. G. Nanoscale Stabilization of New Phases in the PbTe−Sb2Te3 System: PbmSb2nTem+3n Nanocrystals. *Journal of the American Chemical Society* **2013**, *135*, 768–774. https://doi.org/10.1021/ja309626q.

(10) Masadeh, A. S.; Božin, E. S.; Farrow, C. L.; Paglia, G.; Juhas, P.; Billinge, S. J. L.; Karkamkar, A.; Kanatzidis, M. G. Quantitative Size-Dependent Structure and Strain Determination of CdSe Nanoparticles Using Atomic Pair Distribution Function Analysis. *Journal of the American Chemical Society* **2007**, *139*, 10939–10943.

(11) Yang, X.; Masadeh, A. S.; Mcbride, J. R.; Božin, E. S.; Rosenthal, S. J.; Billinge, S. J. L. Confirmation of Disordered Structure of Ultrasmall CdSe Nanoparticles from X-Ray Atomic Pair Distribution Function Analysis. *Phys. Chem. Chem. Phys* **2013**, *15*, 8480. https://doi.org/10.1039/c3cp00111c.

(12) Geng, X.; Cheng, Z.; Wang, S.; Peng, C.; Ullah, A.; Wang, H.; Wu, G. A Data-Driven Machine Learning Approach to Predict the Hardenability Curve of Boron Steels and Assist Alloy Design.

Journal of Materials Science **2022**, *57*, 10755–10768. https://doi.org/10.1007/S10853-022-07132-9.

(13) Li, C.; Li, F.; Liang, J.; Cao, R.; Zhao, Z. Microstructural Evolution and Strain Hardening Mechanism of a Boron-Containing Metastable Austenitic Steel. *Materials Science and Technology* **2019**, *35* (16), 2013–2023. https://doi.org/10.1080/02670836.2019.1661650.

(14) Gupta, S.; Patel, M. K.; Miotello, A.; Patel, N. Metal Boride-Based Catalysts for Electrochemical Water-Splitting: A Review. *Advanced Functional Materials* **2020**, *30*, 1–28. https://doi.org/10.1002/adfm.201906481.

(15) Ni, F.; Ma, Y.; Chen, J.; Luo, W.; Yang, J. Boron-Iron Nanochains for Selective Electrocatalytic Reduction of Nitrate. *Chinese Chemical Letters* **2021**, *32* (6), 2073–2078. https://doi.org/10.1016/j.cclet.2021.03.042.

(16) Bocarsly, J. D.; Levin, E. E.; Humphrey, S. A.; Faske, T.; Donner, W.; Wilson, S. D.; Seshadri, R. Magnetostructural Coupling Drives Magnetocaloric Behavior: The Case of MnB versus FeB. *Chemistry of Materials* **2019**, *31* (13), 4873–4881. https://doi.org/10.1021/acs.chemmater.9b01476.

(17) *ICSD database search. June 2022.*

(18) Li, H.; Wen, P.; Li, Q.; Dun, C.; Xing, J.; Lu, C.; Adhikari, S.; Jiang, L.; Carroll, D. L.; Geyer, S. M. Earth-Abundant Iron Diboride (FeB2) Nanoparticles as Highly Active Bifunctional Electrocatalysts for Overall Water Splitting. *Advanced Energy Materials* **2017**, *7* (17), 1–12. https://doi.org/10.1002/aenm.201700513.

(19) Rades, S.; Kornowski, A.; Weller, H.; Albert, B. Wet-Chemical Synthesis of Nanoscale Iron Boride, XAFS Analysis and Crystallisation to α-FeB. *ChemPhysChem* **2011**, *12* (9), 1756–1760. https://doi.org/10.1002/cphc.201001072.

(20) Rades, S.; Kraemer, S.; Seshadri, R.; Albert, B. Size and Crystallinity Dependence of Magnetism in Nanoscale Iron Boride, α-FeB. *Chemistry of Materials* **2014**, *26* (4), 1549–1552. https://doi.org/10.1021/cm403167a.

(21) Tan, X.; Chai, P.; Thompson, C. M.; Shatruk, M. Magnetocaloric Effect in AlFe2B2: Toward Magnetic Refrigerants from Earth-Abundant Elements. *Journal of the American Chemical Society* **2013**, *135* (25), 9553–9557. https://doi.org/10.1021/ja404107p.

(22) Kádas, K.; Iuşan, D.; Hellsvik, J.; Cedervall, J.; Berastegui, P.; Sahlberg, M.; Jansson, U.; Eriksson, O. AlM2B2 (M = Cr, Mn, Fe, Co, Ni): A Group of Nanolaminated Materials. *Journal of Physics Condensed Matter* **2017**, *29* (155402), 1–11. https://doi.org/10.1088/1361-648X/aa602a.

(23) Levin, E. M.; Jensen, B. A.; Barua, R.; Lejeune, B.; Howard, A.; McCallum, R. W.; Kramer, M. J.; Lewis, L. H. Effects of Al Content and Annealing on the Phases Formation, Lattice Parameters, and Magnetization of AlxFe2B2 (X=1.0,1.1,1.2) Alloys. *Physical Review Materials* **2018**, *2* (3), 34403. https://doi.org/10.1103/PhysRevMaterials.2.034403.

(24) Barua, R.; Lejeune, B. T.; Ke, L.; Hadjipanayis, G.; Levin, E. M.; McCallum, R. W.; Kramer, M. J.; Lewis, L. H. Anisotropic Magnetocaloric Response in AlFe2B2. *Journal of Alloys and Compounds* **2018**, *745*, 505–512. https://doi.org/10.1016/j.jallcom.2018.02.205.

(25) Cedervall, J.; Svante, M.; Sarkar, T.; Delczeg-czirjak, E. K.; Bergqvist, L.; Hansen, T. C.; Beran, P.; Nordblad, P.; Sahlberg, M. Magnetic Structure of the Magnetocaloric Compound AlFe2B2. *Journal of Alloys and Compounds* **2016**, *664*, 784–791. https://doi.org/10.1016/j.jallcom.2015.12.111.

(26) Cedervall, J.; Häggström, L.; Ericsson, T.; Sahlberg, M. Mössbauer Study of the Magnetocaloric Compound AlFe2B2. *Hyperfine Interactions* **2016**, *237* (1), 1–8. https://doi.org/10.1007/s10751-016-1223-7.

(27) Cedervall, J.; Andersson, M. S.; Iuşan, D.; Delczeg-Czirjak, E. K.; Jansson, U.; Nordblad, P.; Sahlberg, M. Magnetic and Mechanical Effects of Mn Substitutions in AlFe2B2. *Journal of Magnetism and Magnetic Materials* **2019**, *482*, 54–60. https://doi.org/10.1016/j.jmmm.2019.03.046.

(28) Alameda, L. T.; Moradifar, P.; Metzger, Z. P.; Alem, N.; Schaak, R. E. Topochemical Deintercalation of Al from MoAlB: Stepwise Etching Pathway, Layered Intergrowth Structures, and Two-Dimensional MBene. *Journal of the American Chemical Society* **2018**, *140*, 8833–8840. https://doi.org/10.1021/jacs.8b04705.

(29) Alameda, L. T.; Lord, R. W.; Barr, J. A.; Moradifar, P.; Metzger, Z. P.; Steimle, B. C.; Holder, C. F.; Alem, N.; Sinnott, S. B.; Schaak, R. E. Multi-Step Topochemical Pathway to Metastable Mo2AlB2 and Related Two-Dimensional Nanosheet Heterostructures. *Journal of the American Chemical Society* **2019**, *141* (27), 10852–10861. https://doi.org/10.1021/jacs.9b04726.

(30) Ade, M.; Hillebrecht, H. Ternary Borides Cr2AlB2 , Cr3AlB4 , and Cr4AlB6 : The First Members of the Series (CrB2)n CrAl with n = 1, 2, 3 and a Unifying Concept for Ternary Borides as MAB-Phases. *Inorganic Chemistry* **2015**, *54* (13), 6122–6135. https://doi.org/10.1021/acs.inorgchem.5b00049.

(31) Elmassalami, M.; Oliveira, D. D. S.; Takeya, H. On the Ferromagnetism of AlFe2B2. *Journal of Magnetism and Magnetic Materials* **2011**, *323* (16), 2133–2136. https://doi.org/10.1016/j.jmmm.2011.03.008.

(32) Jung, W.; Schweitzer, K. The Crystal Structures of Al2Ru3B2 and Al3Ru4B2 Ternary Borides. *Zeitschrift für Kristallographie* **1986**, *174* (1–4), 109–110.

(33) Wang, J.; Ye, T.-N.; Gong, Y.; Wu, J.; Miao, N.; Tada, T.; Hosono, H. Discovery of Hexagonal Ternary Phase Ti2InB2 and Its Evolution to Layered Boride TiB. *Nature Communications* **2019**, *10* (1), 2284–2292. https://doi.org/10.1038/s41467-019-10297-8.

(34) Zhou, J.; Palisaitis, J.; Halim, J.; Dahlqvist, M.; Tao, Q.; Persson, I.; Hultman, L.; Persson., P. O. Å.; Rosen, J. Boridene: Two-Dimensional Mo4/3B2-x with Ordered Metal Vacancies Obtained by Chemical Exfoliation. *Science* **2021**, *373* (6556), 801–805.

(35) Helmer, P.; Halim, J.; Zhou, J.; Mohan, R.; Wickman, B.; Björk, J.; Rosen, J.; Helmer, P.; Halim, J.; Zhou, J.; Björk, J.; Rosen, J.; Mohan, R.; Wickman, B. Investigation of 2D Boridene from First Principles and Experiments. *Advanced Functional Materials* **2022**, *32* (14), 2109060. https://doi.org/10.1002/adfm.202109060.

(36) Guo, Z.; Sun, Z. New Two-Dimensional Transition Metal Borides for Li Ion Batteries and Electrocatalysis. *Journal of Materials Chemistry A* **2017**, *5*, 23530–23535. https://doi.org/10.1039/c7ta08665b.

(37) Liu, J.; Li, S.; Yao, B.; Hu, S.; Zhang, J.; Yu, W.; Zhou, Y. Rapid Synthesis and Characterization of a Nanolaminated Fe2AlB2 Compound. *Journal of Alloys and Compounds* **2018**, *766*, 488–497. https://doi.org/10.1016/j.jallcom.2018.06.352.

(38) Bennett, S. P.; Kota, S.; ElBidweihy, H.; Parker, J. F.; Hanner, L. A.; Finkel, P.; Barsoum, M. W. Magnetic and Magnetocaloric Properties of Fe2AlB2 Synthesized by Single-Step Reactive Hot Pressing. *Scripta Materialia* **2020**, *188*, 244–248. https://doi.org/10.1016/j.scriptamat.2020.07.042.

(39) Tsurin, V. A.; Turkhan, Y. E.; Kazantsev, V. A.; Fedorenko, V. V.; Novikov, S. I.; Barinov, V. A.; Surikov, V. T.; Dorofeev, G. A. α-FeB: Structure, Hyperfine Interactions, and Magnetic Properties. *Journal of Metals and Metallography* **2003**, *96*, 36.

(40) Deyoung, D. B.; Barnes, R. G. A Mössbauer Effect Study of 57Fe in Transition Metal Monoborides. *The Journal of Chemical Physics* **1975**, *62* (5), 1726–1738. https://doi.org/10.1063/1.430698.

(41) Jothi, P. R.; Yubuta, K.; Fokwa, B. P. T. A Simple, General Synthetic Route toward Nanoscale Transition Metal Borides. *Advanced Materials* **2018**, *30* (14), 2–7. https://doi.org/10.1002/adma.201704181.

(42) Dorofeev, G. A.; Ovechkin, L. V.; Elsukov, E. P.; Barinov, V. A. Local Magnetic Structure of α-Iron Monoboride Produced by Mechanical Fragmentation. *Journal of Metals and Metallography* **1993**, *76* (4), 107–113.

(43) Yelsukov, E. P.; Dorofeev, G. A.; Barinov, V. A. Mössbauer Study of Solid State Reactions under Mechanical Grinding of the Fe2B and FeB Borides. *Czechoslovak Journal of Physics* **1997**, *47* (5), 499–506.

(44) Kanaizuka, T. Interpretation of Mössbauer Spectra of β-FeB and Its Low Temperature Modification, α-FeB. *Physica Status Solidi* **1982**, *69* (2), 739–744. https://doi.org/10.1002/PSSA.2210690237.

(45) Mohn, P. The Calculated Electronic and Magnetic Properties of the Tetragonal Transition-Metal Semi-Borides. *Journal of Physics C: Solid State Physics* **1988**, *21* (15), 2841–2851. https://doi.org/10.1088/0022-3719/21/15/016.

(46) Fruchart, R. Cementites of Boron, Iron Borides, and the Nickel Boride, Ni3B. *Annalen der Chemie* **1959**, *4*, 1247.

(47) Barinov, V. A.; Dorofeev, G. A.; Ovechkin, L. V.; Elsukov, E. P.; Ermakov, A. E. Structure and Magnetic Properties of the α-FeB Phase Obtained by Mechanical Working. *physica status solidi (a)* **1991**, *123* (2), 527–534. https://doi.org/10.1002/PSSA.2211230217.

(48) Kanaizuka, T. Phase Diagram of Pseudobinary CrB-MnB and MnB-FeB Systems: Crystal Structure of the Low-Temperature Modification of FeB. *Journal of Solid State Chemistry* **1982**, *41* (2), 195–204. https://doi.org/10.1016/0022-4596(82)90202-X.

(49) Casas-Cabanas, M.; Rodríguez-Carvajal, J.; Palacín, M. R. FAULTS, a New Program for Refinement of Powder Diffraction Patterns from Layered Structures. *Zeitschrift für Kristallographie* **2006**, *23*, 144–145.

(50) Casas-Cabanas, M.; Reynaud, M.; Rikarte, J.; Horbach, P.; Rodríguez-Carvajal, J. FAULTS: A Program for Refinement of Structures with Extended Defects. *J. Appl. Cryst* **2016**, *49*, 2259–2269. https://doi.org/10.1107/S1600576716014473.

(51) Toby, B. H.; Von Dreele, R. B. GSAS-II: The Genesis of a Modern Open-Source All Purpose Crystallography Software Package. *J. Appl. Cryst* **2013**, *46*, 544–549. https://doi.org/10.1107/S0021889813003531.

(52) Portehault, D.; Devi, S.; Beaunier, P.; Gervais, C.; Giordano, C.; Sanchez, C.; Antonietti, M. A General Solution Route toward Metal Boride Nanocrystals. *Angewandte Chemie - International Edition* **2011**, *50* (14), 3262–3265. https://doi.org/10.1002/anie.201006810.

(53) Wei, Y.; Liu, Z.; Ran, S.; Xia, A.; Yi, T. F.; Ji, Y. Synthesis and Properties of Fe-B Powders by Molten Salt Method. *Journal of Materials Research* **2017**, *32* (4), 883–889. https://doi.org/10.1557/jmr.2017.38.

(54) Kapfenberger, C.; Albert, B.; Pöttgen, R.; Huppertz, H. Structure Refinements of Iron Borides Fe2B and FeB. *Zeitschrift für Kristallographie-Crystalline Materials* **2006**, *221*, 477–481. https://doi.org/10.1524/zkri.2006.221.5.

(55) Gouget, G.; Beaunier, P.; Portehault, D.; Sanchez, C. New Route toward Nanosized Crystalline Metal Borides with Tuneable Stoichiometry and Variable Morphologies. *Faraday Discussions* **2016**, *191*, 511–525. https://doi.org/10.1039/c6fd00053c.

(56) Hirt, S.; Hilfinger, F.; Hillebrecht, H. Synthesis and Crystal Structures of the New Ternary Borides Fe3Al2B2 and Ru9Al3B8 and the Confirmation of Ru4Al3B2 and Ru9Al5B8-x (x ≈ 2). *Zeitschrift fur Kristallographie - Crystalline Materials* **2018**, *233* (5), 295–307. https://doi.org/10.1515/zkri-2017-2095.

(57) Altomare, A.; Corriero, N.; Cuocci, C.; Falcicchio, A.; Moliterni, A.; Rizzi, R. EXPO Software for Solving Crystal Structures by Powder Diffraction Data: Methods and Application. *Cryst. Res. Technol* **2015**, *50* (9), 737–742. https://doi.org/10.1002/crat.201500024.

(58) Hohnke, D.; Parthé, E. FeB and CrB Type Structures of Monosflieides and Germanides. *Acta Cryst* **1966**, *20*, 582.

(59) Klepp, K.; Parthé, E. Yttrium-Nickel YNi with the FeB Structure Type. *Acta Crystallographica* **1980**, *B36*, 3093–3094.

(60) Klepp, K.; Parthé, E. Orthorhombic Gadolinium Nickel Silicide Gd3NiSi 2 with a Filled-up Hf3P2 Structure Type. *Acta Crystallographica* **1981**, *B37*, 1500–1504.

(61) Le Roy, J.; Moreau, J.; Paccard, D.; Parthé, E. Structures of the Rare-Earth-Platinum Compounds R7Pt3, R2Pt, RsPt 3 and RPt. *Acta Crystallographica* **1978**, *B34*, 9–13.

(62) Parthé, E. The CrB and Related Structure Types Interpreted by Periodic Unit-Cell Twinning of Close-Packed Structures. *Acta Crystallographica* **1976**, *B32*, 2813–2818.

(63) Rades, S. Synthese Und Charakterisierung von Nanopartikeln Im System Eisen-Bor, 2012.

(64) Serrano-Sevillano, J.; Charbonnier, V.; Madern, N.; Latroche, M.; Magén, C.; Serin, V.; Monnier, J.; Casas-Cabanas, M.; Zhang, J. Quantification of Stacking Faults in ANi y (A = Rare Earth or Mg, y = 3.5 and 3.67) Hydrogen Storage Materials. *Chem. Mater* **2022**, *34*, 4568–4576. https://doi.org/10.1021/acs.chemmater.2c00408.

(65) Perez, A. J.; Batuk, D.; Saubanère, M.; Rousse, G.; Foix, D.; McCalla, E.; Berg, E. J.; Dugas, R.; Van Den Bos, K. H. W.; Doublet, M. L.; Gonbeau, D.; Abakumov, A. M.; Van Tendeloo, G.; Tarascon, J. M. Strong Oxygen Participation in the Redox Governing the Structural and Electrochemical Properties of Na-Rich Layered Oxide Na2IrO3. *Chemistry of Materials* **2016**, *28* (22), 8278–8288. https://doi.org/10.1021/acs.chemmater.6b03338.

(66) Mortemard de Boisse, B.; Reynaud, M.; Ma, J.; Kikkawa, J.; Nishimura, S. ichi; Casas-Cabanas, M.; Delmas, C.; Okubo, M.; Yamada, A. Coulombic Self-Ordering upon Charging a Large-Capacity Layered Cathode Material for Rechargeable Batteries. *Nature Communications* **2019**, *10* (1), 1–7. https://doi.org/10.1038/s41467-019-09409-1.

(67) Masese, T.; Miyazaki, Y.; Rizell, J.; Kanyolo, G. M.; Chen, C. Y.; Ubukata, H.; Kubota, K.; Sau, K.; Ikeshoji, T.; Huang, Z. D.; Yoshii, K.; Takahashi, T.; Ito, M.; Senoh, H.; Hwang, J.; Alshehabi, A.; Matsumoto, K.; Matsunaga, T.; Fujii, K.; Yashima, M.; Shikano, M.; Tassel, C.; Kageyama, H.; Uchimoto, Y.; Hagiwara, R.; Saito, T. Mixed Alkali-Ion Transport and Storage in Atomic-Disordered Honeycomb Layered NaKNi2TeO6. *Nature Communications* **2021**, *12* (1), 1–16. https://doi.org/10.1038/s41467-021-24694-5.

(68) Treacy, M. M. J.; Deem, M. W.; Newsam, J. M. How DIFFaX Works. In *DIFFaX Manual*; 2005; pp 48–50.

(69) Kanai, T.; Ka, Z. U. Phase Diagram of Pseudobinary CrB-MnB and MnB-FeB Systems: Crystal Structure of the Low-Temperature Modification of FeB. *Journal of Solid State Chemistry* **1982**, *41*, 195–204.

(70) Dey, M.; Javaid, S.; Clifford, D.; Sharma, V.; Barua, R.; Gupta, S. Synthesis of Nanolayered Ternary Borides Powders (MAB Phases) by Sustainable Molten Salt Shielded Synthesis/Sintering (MS3) Process. *Journal of Materials Science* **2022**, *57* (4), 2436–2454. https://doi.org/10.1007/s10853-021-06779-0.

TOC

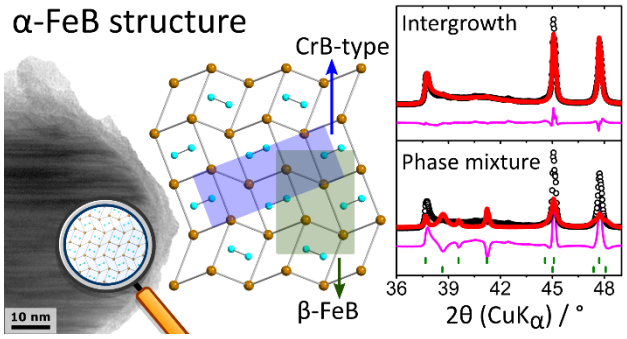
α-FeB structure
CrB-type
β-FeB
10 nm
Intergrowth
Phase mixture
36
39
42
45
48
2θ (CuKα) / °